Nanoscale

PAPER

View Article Online
View Journal | View Issue

Cite this: *Nanoscale*, 2024, **16**, 4025

Elucidating the reversible and irreversible self-assembly mechanisms of low-complexity aromatic-rich kinked peptides and steric zipper peptides†

Zenghui Lao,‡[a] Yiming Tang,‡[a] Xuewei Dong,[b] Yuan Tan,[a] Xuhua Li,[c] Xianshi Liu,[a] Le Li,[a] Cong Guo *[d] and Guanghong Wei *[a]

Many RNA-binding proteins such as fused-in sarcoma (FUS) can self-assemble into reversible liquid droplets and fibrils through the self-association of their low-complexity (LC) domains. Recent experiments have revealed that SYG-rich segments in the FUS LC domains play critical roles in the reversible self-assembly behaviors of FUS. These FUS LC segments alone can self-assemble into reversible kinked fibrils, which are markedly different from the canonical irreversible steric zipper β-sheet fibrils. However, the molecular determinants underlying the reversible and irreversible self-assembly are poorly understood. Herein we conducted extensive all-atom and coarse-grained molecular dynamics simulations of four representative hexapeptides: two low-complexity aromatic-rich kinked peptides from the amyotrophic lateral sclerosis-related FUS protein, FUS_{37-42} (SYSGYS) and FUS_{54-59} (SYSSYG); and two steric zipper peptides from Alzheimer's-associated Aβ and Tau proteins, $Aβ_{16-21}$ (KLVFFA) and $Tau_{306-311}$ (VQIVYK). We dissected their reversible and irreversible self-assembly dynamics, predicted their phase separation behaviors, and elucidated the underpinning molecular interactions. Our simulations showed that alternating stickers (Tyr) and spacers (Gly and Ser) in FUS_{37-42} and FUS_{54-59} facilitate the formation of highly dynamic coil-rich oligomers and lead to reversible self-assembly, while consecutive hydrophobic residues of LVFF in $Aβ_{16-21}$ and IVY in $Tau_{306-311}$ act as hydrophobic patches, favoring the formation of stable β-sheet-rich oligomers and driving the irreversible self-assembly. Intriguingly, we found that FUS_{37-42} and FUS_{54-59} peptides, possessing the same amino acid composition and the same number of sticker and spacer residues, display differential self-assembly propensities. This finding suggests that the self-assembly behaviors of FUS peptides are fine-tuned by the site-specific patterning of spacer residues (Ser and Gly). This study provides significant mechanistic insights into reversible and irreversible peptide self-assembly, which would be helpful for understanding the molecular mechanisms underlying the formation of biological liquid condensates and pathological solid amyloid fibrils.

Received 11th October 2023,
Accepted 29th January 2024

DOI: 10.1039/d3nr05130g

rsc.li/nanoscale

Introduction

Fibrillary deposits are the hallmark of many neurodegenerative disorders,[1,2] such as Alzheimer's disease associated with the fibrillary aggregates of Aβ and Tau.[3–5] Amyloid fibrils (also known as steric zipper β-sheet fibrils) share cross-β architecture, with extended β-strands stacking along the fibril axis into a β-sheet and the side chains of mating sheets interdigitating with each other.[6–8] Attributed to their highly ordered intermolecular backbone hydrogen bonds (H-bonds) and complementary dry zipper interface, steric zipper β-sheet fibrils are stable and present strong resistance to dissociation under harsh conditions, such as being in the presence of chemical denaturants[9] or at an elevated temperature.[10]

In addition to the highly stable cross-β fibrils (irreversible fibrils), in recent years, labile kinked β-sheet fibrils with

[a]*Department of Physics, State Key Laboratory of Surface Physics, Key Laboratory for Computational Physical Sciences (Ministry of Education), Fudan University, Shanghai, China. E-mail: ghwei@fudan.edu.cn*
[b]*Center for Soft Condensed Matter Physics and Interdisciplinary Research & School of Physical Science and Technology, Soochow University, Suzhou 215006, Jiangsu, China*
[c]*MOE Key Laboratory for Nonequilibrium Synthesis and Modulation of Condensed Matter, School of Physics, Xi'an Jiaotong University, Xi'an 710049, China*
[d]*Department of Physics and International Centre for Quantum and Molecular Structures, College of Sciences, Shanghai University, Shanghai, China. E-mail: congguo@shu.edu.cn*

†Electronic supplementary information (ESI) available. See DOI: https://doi.org/10.1039/d3nr05130g

‡These authors contributed equally to this work.

thermal-responsive reversibility (reversible fibrils) have been reported to be formed by many RNA binding proteins, such as fused-in sarcoma (FUS),[11–13] TAR DNA-binding protein 43 (TDP-43)[14,15] and heterogeneous nuclear ribonucleoprotein A1 (hnRNPA1)[13,16] and A2 (hnRNPA2).[17] These proteins are capable of undergoing liquid–liquid phase separation (LLPS) to form liquid biomolecular condensates.[18,19] On the one hand, LLPS is identified as the formation mechanism of the membrane-less organelles (MLOs, composed of proteins and RNAs)[20–25] and is involved in many biological cellular functions.[26–28] On the other hand, LLPS plays a critical role in the formation of toxic aggregates in diseases such as amyotrophic lateral sclerosis (ALS)[29–33] and frontotemporal lobar degeneration (FTLD).[34–37] Under abnormal conditions, such as mutations or continuous external stimuli, the droplets formed *via* LLPS can turn into solid fibrillary aggregates, a process which is called liquid-to-solid phase transition (LSPT).[30,37] The amyloid fibrils are a common end-stage product of LSPT.[7] Recently, the structure of the reversible fibril formed by the fibril core of the FUS low complexity (FUS LC) domain has been determined by solid state nuclear magnetic resonance (ssNMR).[11] This fibril core consists of residues 35–95 of FUS ($FUS_{35–95}$), a 61-residue segment. The $FUS_{35–95}$ fibril, unlike the steric zipper β-sheet fibril, is labile for the lack of intermolecular side chain hydrophobic interactions (or tight interdigitation).[38] Apart from through maturation or aging (the time-dependent coarsening and loss of dynamicity) of a liquid-like droplet by RNA binding proteins such as FUS, pathogenic fibrils can also be formed by proteins such as Aβ directly through irreversible aggregation without LLPS, which is termed liquid–solid phase separation (LSPS).[39]

In addition to full-length proteins and their LC domains, short peptides are able to phase separate, forming liquid condensates[40–43] and reversible or irreversible fibrils.[12,13,15]

Cong Guo

Cong Guo is an associate professor in the Department of Physics, College of Sciences at Shanghai University, China. She obtained her PhD from Fudan University under the supervision of Prof. Guanghong Wei in 2014 and worked as a postdoctoral fellow under the supervision of Prof. Huan-xiang Zhou at Florida State University and then Prof. Anant Paravastu at Georgia Institute of Technology before joining Shanghai University in December 2017. Her research focuses on understanding the molecular mechanism of the assembly of peptides into ordered nanostructures or amyloid fibrils and the regulation of pathological fibrillization by endogenous proteins with molecular dynamics simulations.

Recent crystal structure studies of short peptides have provided different structural properties of the two types of fibrils.[39] Unlike the irreversible fibrils, the structures of reversible fibrils are organized in kinked strands perpendicular to the fibril spine, or extended β-strands with a hydrous sheet interface, or a stacking pattern with Asp residues from individual β-strands aligned along the fibril spine.[7,12,13,16] For example, fibrils of $FUS_{37–42}$ (PDB ID: 5XSG) comprise kinked strands without extended β sheets (Fig. S1A†), and fibrils of $FUS_{54–59}$ (PDB ID: 5XRR) consist of pairs of β-sheets with a hydrophilic interface (Fig. S1B†).[12] In contrast, the irreversible fibril structures of $A\beta_{16–21}$ (PDB ID: 3OW9)[44] and $Tau_{306–311}$ (PDB ID: 2ON9)[45] (Fig. S1C ad S1D†) are composed of stacking β-strands and have large hydrophobic interfaces between β-sheets and surface complementarity. Eisenberg's group also solved the fibril structures of several segments from FUS, hnRNPA1 and nup98 proteins,[13] named LARKS (low-complexity aromatic-rich kinked segment). LARKS forms reversible hydrogel, rather than irreversible fibrils.[15]

Reversible fibrils are easily dissociated by heating or adding detergent.[12,13,16] In the thermostability experiments performed by Liu's group,[12] it was found that fibrils formed from two tandem (S/G)Y(S/G) motifs of FUS, namely $_{37}$SYSGYS$_{42}$ ($FUS_{37–42}$) and $_{54}$SYSSYG$_{59}$ ($FUS_{54–59}$) at 4 °C dissolved upon heating to room temperature or higher. When cooled down back to 4 °C, both $FUS_{37–42}$ and $FUS_{54–59}$ fibrils were formed again.[12] In contrast, the amyloid fibrils (termed irreversible fibrils) of $A\beta_{16–21}$ (Ace-$_{16}$KLVFFA$_{21}$) and $Tau_{306–311}$ (Ace-$_{306}$VQIVYK$_{311}$) remained intact during the heating and cooling processes, displaying high thermostability.[12]

In spite of the structural characteristics and thermal stabilities of reversible and irreversible fibrils being well studied experimentally, the dynamic properties and phase behaviors of those reversible/irreversible self-assembling peptides as well as their underlying molecular mechanisms remain largely elusive. In this study, we investigated the reversible/irreversible self-assembly process and predicted the LLPS/LSPS of four hexapeptides, namely $FUS_{37–42}$, $FUS_{54–59}$, $A\beta_{16–21}$ and $Tau_{306–311}$, using both all-atom molecular dynamic (AA-MD) and coarse-grained MD (CG-MD) simulations combined with explicit water solvents. We dissected the main differences in the dynamic and structural properties of reversible and irreversible peptide self-assembly, characterized the phase behaviors, and elucidated the underlying molecular interactions. Our computational work provides atomic insights into the reversible and irreversible self-assembly of short fibril-forming peptides, which may be helpful for the in-depth mechanistic understanding of LLPS and LSPS of proteins.

Models and methods

System setup

We selected four representative short peptides as our study models, two from the ALS-related FUS protein, $FUS_{37–42}$ ($_{37}$SYSGYS$_{42}$) and $FUS_{54–59}$ ($_{54}$SYSSYG$_{59}$),[12] and another two from the Alzheimer's-associated Aβ/Tau proteins, $A\beta_{16–21}$

(Ace-$_{16}$KLVFFA$_{21}$)[44] and Tau$_{306–311}$ (Ace-$_{306}$VQIVYK$_{311}$).[45] We simulated a total of 12 systems for the four peptides: four all-atom fibril systems, four all-atom oligomer systems, and four coarse-grained oligomer systems. All the systems together with the simulation setups are provided in Table 1.

All-atom fibril systems. The initial fibril structures of the four hexapeptides used in our study consisted of 12 peptide chains (Fig. S1†). They were taken from the fibril structures of FUS$_{37–42}$ (PDB ID: 5XSG) and FUS$_{54–59}$ (PDB ID: 5XRR) solved by Luo *et al.*,[12] and Aβ$_{16–21}$ (PDB ID: 3OW9) and Tau$_{306–311}$ (PDB ID: 2ON9) fibril structures determined by the Eisenberg group.[44,45] Aβ$_{16–21}$ and Tau$_{306–311}$ fibrils were acetylated at the N-terminal to keep peptides electrostatically neutral, consistent with capped peptides used for the thermostability measurements by Liu's group.[12] These peptide fibrils were placed in the center of a box with a side length of ∼7.0 nm.

All-atom oligomer systems. The initial state of each oligomer system consisted of six monomers with random coil conformations, with each monomer randomly placed in the simulation box with dimensions of ∼8.5 × 8.5 × 8.5 nm^3. Peptide monomers were first constructed using PyMOL[46] in extended coil states, then simulated under 410 K for 50 ns.

Coarse-grained oligomer systems. In the initial state of each system, 200 monomers were randomly displaced in an aqueous simulation box containing about 43 000 water beads and 527 Na^+ and 527 Cl^- ions (∼0.15 M NaCl). The simulation box has a size of ∼18 × 18 × 18 nm^3.

AA-MD simulations

AA-MD simulations were performed using the GROMACS-2016.4 software package[47] in combination with the AMBER99SB-ILDN force field[48] and TIP3P water model. Na^+ and Cl^- ions at a physiological concentration of 0.15 M were added to all the simulation boxes. We used the Verlet cutoff scheme for neighbor searching and the particle mesh Ewald (PME) method[49,50] for electrostatic interaction calculations. A real-space cutoff of 1.4 nm was used for electrostatic interaction. The cutoff for van der Waals interaction was also set as 1.4 nm. Periodic boundary conditions were applied for all simulations. Before the production run of the MD simulations, all the systems were sequentially equilibrated under an NVT (310 K) ensemble for 100 ps, and then under an NPT (310 K and 1 bar) ensemble for 100 ps.[51] After that, each simulation was run for 500 ns, with an integration time step of 2 fs. Velocity rescale[52] and the Parrinello-Rahman[53] methods were used for temperature and pressure coupling, respectively. To obtain statistically significant results, two independent simulations at 310 K were conducted for each fibril system, and five independent simulations at 310 K were performed for each of the oligomer systems. To examine the fluidity of the peptides at a higher temperature, another 500 ns simulation was conducted for each of the four oligomer systems at 340 K, starting from the final state of the MD simulation at 310 K.

CG-MD simulation

All CG-MD simulations were performed using the GROMACS-2018.3 software package. The peptides were described using the MARTINI coarse-grained force field (version 2.2)[54,55] with modifications described as follows. Electrostatic interactions were calculated using the reaction field method[56] with a real-space cut-off of 1.4 nm in the CG-MD simulations. The other simulation setups were the same as those used in the AA-MD simulations. Three independent 6 μs simulations were conducted for each system to ensure that each of them reached equilibrium. The previous literature has reported the overestimation of inter-residue interaction strength using the MARTINI forcefield,[57–59] especially for Ser and Thr residues. Several groups have utilized a scaling factor α to adjust the pair-interaction well depth, which is aimed at reproducing experimental observations.[57,58] As FUS$_{37–42}$ and FUS$_{54–59}$ peptides are enriched in Ser residues, rescaling the pair interaction is crucial for accurately characterizing their assembly capabilities. However, the selection of the α value is system-dependent, and experimental data for the condensates formed by these two FUS segments are not available. In a recent work, the Hummer group has shown that FUS-LCD condensation occurs above a critical α value of 0.6, and the experimental densities

Table 1 A summary of all the systems and simulation setups

Systems[a]			Number of chains	Number of atoms/beads	Temperature	Simulation time
All-atom	Fibrils	FUS$_{37–42}$	12	33 575	310 K	500 ns × 2
		FUS$_{54–59}$		33 584		
		Aβ$_{16–21}$		33 653		
		Tau$_{306–311}$		33 620		
	Oligomers	FUS$_{37–42}$	6	60 134	310 K	310 K: 500 ns × 5
		FUS$_{54–59}$		60 137		
		Aβ$_{16–21}$		60 161	340 K	340 K: 500 ns × 1
		Tau$_{306–311}$		60 203		
Coarse-grained	Condensates	FUS$_{37–42}$	200	46 854	310 K	6 μs × 3
		FUS$_{54–59}$		46 854		
		Aβ$_{16–21}$		47 054		
		Tau$_{306–311}$		46 854		

[a] FUS$_{37–42}$: $_{37}$SYSGYS$_{42}$; FUS$_{54–59}$: $_{54}$SYSSYG$_{59}$; Aβ$_{16–21}$: Ace-$_{16}$KLVFFA$_{21}$; Tau$_{306–311}$: Ace-$_{306}$VQIVYK$_{311}$.

of both the dilute and dense phases were accurately replicated at α = 0.65.[58] In spite of a much shorter sequence length, $FUS_{37–42}$ and $FUS_{54–59}$ have been identified as two reversible amyloid cores, which mediate the dynamic assembly of FUS LCD.[12] We thus infer that α = 0.65 may also be suitable for studying the self-assembly process of $FUS_{37–42}$ and $FUS_{54–59}$. To test this hypothesis, we selected six α values (0.2, 0.4, 0.5, 0.6, 0.65, and 0.8) and performed short (600 ns) simulations to compare their performance in characterizing the assembly capability of the peptides. The scaling was performed following the method of Stark *et al.*[55] by down-scaling the van der Waals parameters between Ser pseudo-atoms and the backbone beads of all residues, $\varepsilon_\alpha = \varepsilon_0 + \alpha(\varepsilon_{original} - \varepsilon_0)$. A value of α = 0 corresponds to a repulsion-dominated interaction in the MARTINI model (ε_0 = 2 kJ mol^{-1}), and a value of α = 1 recovers the full interaction in the MARTINI force field ($\varepsilon_1 = \varepsilon_{original}$). The results suggest that $FUS_{37–42}$ and $FUS_{54–59}$ presented increasing assembly capability with increasing scaling factor values (Fig. S2†). They displayed weak assembly capabilities at low α values (<0.6), especially $FUS_{37–42}$, while they presented higher assembly ability than $A\beta_{16–21}$ and $Tau_{306–311}$ at a high α value (0.8). At a moderate α value of 0.65, $FUS_{37–42}$ and $FUS_{54–59}$ possessed a certain degree of assembly capability, which was lower than that of $A\beta_{16–21}$ and $Tau_{306–311}$ in good agreement with previous experimental observations.[12] We thus selected 0.65 as the scaling factor for performing the coarse-grained simulations. To offer a quantitative comparison with all-atom simulations, we conducted coarse-grained simulations for each of the four peptides starting from six randomly dispersed peptide chains. At a scaling factor of α = 0.65, the collapse degree and SASA fluctuation values predicted by coarse-grained simulations were of the same order of magnitude as those predicted by the all-atom simulations (Fig. S3†). Moreover, both simulations predicted that $FUS_{37–42}$/$FUS_{54–59}$ possessed lower assembly capability and higher liquidity than $A\beta_{16–21}$/$Tau_{306–311}$.

Analysis methods

Data analysis was performed using the tools implemented in the GROMACS software package and our in-house developed codes. For data analysis of the AA-MD simulations, an atomic contact was defined as being when two aliphatic carbon atoms were within 0.54 nm of one another or when any other two heavy atoms came within 0.46 nm.[60–62] When two monomers were located with a minimum distance between heavy atoms of less than 0.54 nm, they were regarded as belonging to one cluster. The intra- and inter-chain dihedral correlations were evaluated following previous literature.[63] The correlation coefficients between two dihedrals (x and y) were calculated utilizing the method put forward by Jammalamadaka and Sengupta,[64] using the following equation:

$$\rho_{xy}^{\text{circular}} = \frac{\sum_{i=1}^{N} \sin(x_i - \bar{x}) \cdot \cos(y_i - \bar{y})}{\sqrt{\sum_{i=1}^{N} \sin^2(x_i - \bar{x}) \cdot \sum_{i=1}^{N} \sin^2(y_i - \bar{y})}}$$

A hydrogen bond (H-bond) was considered to be formed on the basis of two conditions:[65–67] (1) the distance between the H-bond donor (D) and the acceptor (A) is less than 0.35 nm, and (2) the angle of D–H···A is larger than 150°. The secondary structure was analyzed using the DSSP tool.[68] The end-to-end distance of a monomer refers to the distance between the first and the last Cα atoms of the monomer. Two aromatic residues were in the π–π stacking state when the distance between the centroids of two aromatic rings was less than 0.7 nm.[69] Three different types of stacking patterns were defined according to the angles of the two aromatic rings: 0°–30° for parallel, 30°–60° for herringbone, and 60°–90° for T-shape. The statistical results of the AA-MD simulations were all based on the data from 300 to 500 ns.

In the data analysis of CG-MD simulations, two monomers were considered to have molecular contact if their minimum distance was less than 0.6 nm. In accordance with our recent study, the aggregation propensity of each peptide was characterized using the collapse degree and the clustering degree.[43] The collapse degree was defined as the ratio of SASA of all hexapeptide molecules in the initial state to their SASA in the final configuration.[70] The clustering degree was defined by molecules in clusters divided by the total number of molecules in the system.[43] The fluidity of an aggregate was characterized using the fluctuation of SASA, fluctuation of the clustering degree and the exchange rate of the interactions.[43] The statistical results of the CG-MD simulations were all based on data from 3 to 6 μs. All the structure representations were drawn using the VMD program[71] or PyMOL.[46]

Results and discussion

Fibrils formed by the four hexapeptides display different thermoresponsive stabilities

We first examined the structural stability of the preformed fibrils of the $FUS_{37–42}$, $FUS_{54–59}$, $A\beta_{16–21}$ and $Tau_{306–311}$ peptides. Two independent 500 ns simulations were carried out at 310 K for each fibril system and the results are shown in Fig. 1. It is noted that the structures of the $FUS_{37–42}$/$FUS_{54–59}$ fibril and the $A\beta_{16–21}$/$Tau_{306–311}$ fibril were solved at 4 °C and 18 °C,[12,44,45] which were lower than our simulation temperature (310 K). As seen in Fig. 1a and b, the Cα-root-mean-square-deviation (Cα-RMSD) and the radius of gyration (R_g) values of both $FUS_{37–42}$ and $FUS_{54–59}$ far exceeded those of $A\beta_{16–21}$ and $Tau_{306–311}$ and fluctuated considerably, indicating that the fibril structures of $FUS_{37–42}$ and $FUS_{54–59}$ were much less stable than those of the $A\beta_{16–21}$ and $Tau_{306–311}$ fibril structures. The fibril structures of $FUS_{37–42}$ and $FUS_{54–59}$ were completely disrupted in the final state. In contrast, both the Cα-RMSD and R_g curves of $A\beta_{16–21}$ and $Tau_{306–311}$ maintained a plateau at small values (Fig. 1a and b), although the fibril structures of $A\beta_{16–21}$ and $Tau_{306–311}$ were twisted and the β-sheet contents decreased a bit (Fig. 1d). Then, the side chain dynamics of the four systems were analyzed by calculating the rate of side chain dihedral angle (χ_1) transition between the

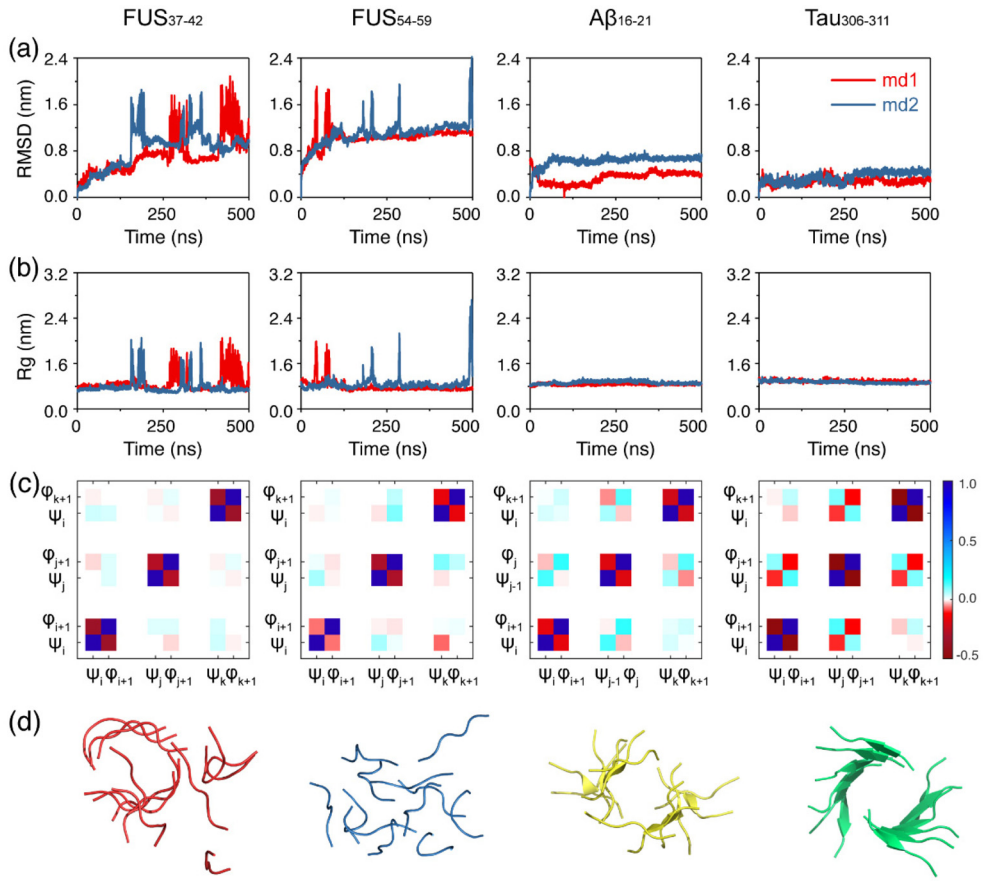

Fig. 1 Thermostability of the preformed FUS_{37-42}, FUS_{54-59}, $A\beta_{16-21}$ and $Tau_{306-311}$ fibrils. Time evolution of (a) RMSD and (b) R_g values of the FUS_{37-42}, FUS_{54-59}, $A\beta_{16-21}$ and $Tau_{306-311}$ fibrils. (c) The dihedral angle correlation coefficients within and between the peptide chains in the four fibril systems. (d) Snapshots of the final states of the four fibril systems. Peptides were drawn using PyMOL.

C^{γ}–*exo* and C^{γ}–*endo* conformations.[72] It can be seen from Fig. S4† that FUS_{37-42} and FUS_{54-59} had much higher χ_1 transition rates (>2.0) than $A\beta_{16-21}$ and $Tau_{306-311}$ (<1.2), suggesting a much higher degree of side chain dynamics of the LARKS peptides. This high degree of dynamics likely played a role in the low stability of the FUS_{37-42} and FUS_{54-59} fibrils. The previous literature has revealed that correlated backbone motions are one of the fundamental properties of the β-sheet.[63] To investigate the backbone correlation of the four fibrils, we calculated the circular cross-correlation coefficients of main chain dihedrals within and between the fibril chains (Fig. 1c). The definitions of the dihedral angles for parallel and antiparallel β-strands are given in Fig. S5.† Strong local anticorrelations are observed between the φ and ψ values of each peptide chain in all of the four systems. This anticorrelation is consistent with the previous literature and indicates the rigidity of the peptide plane, which couples the motion of the dihedral angles while preserving the structure of the strands. Strong inter-chain correlations are also observed between the adjacent chains in the $A\beta_{16-21}$ and $Tau_{306-311}$ systems, indicating the stability of their fibrils. Interestingly, in the $A\beta_{16-21}$ system φ–φ and ψ–ψ dihedral pairs are correlated while the φ–ψ pair is anticorrelated, and *vice versa* in the $Tau_{306-311}$ system. This is due to the antiparallel and parallel nature of the $A\beta_{16-21}$ and $Tau_{306-311}$ β-sheets. In contrast, the inter-chain correlations of the FUS_{37-42} and FUS_{54-59} systems are much weaker, further demonstrating the instability of their fibrils. The computationally observed lower stability of the LARK segments FUS_{37-42}/FUS_{37-42} than that of the $A\beta_{16-21}$/$Tau_{306-311}$ peptides is consistent with previous experimental observations,[12] demonstrating the accuracy and suitability of the force field and the methodology that we used.

The FUS_{37-42}/FUS_{54-59} peptides form highly dynamic oligomers, whereas the $A\beta_{16-21}$/$Tau_{306-311}$ peptides assemble into stable oligomers

After the structural stability examination of the fibril structures, we investigated the self-assembly processes of the four hexapeptides using AA-MD simulations. It is shown in Fig. 2a that the numbers of clusters of FUS_{37-42} and FUS_{54-59} vary during the oligomerization process. The monomers of FUS_{37-42} and FUS_{54-59} gathered together first, then were separated, and came together again, indicating that their self-assembly processes are highly dynamic, and their aggregates are labile and easy to dissolve. In the $A\beta_{16-21}$ and $Tau_{306-311}$ systems, in marked contrast, most monomers self-assembled

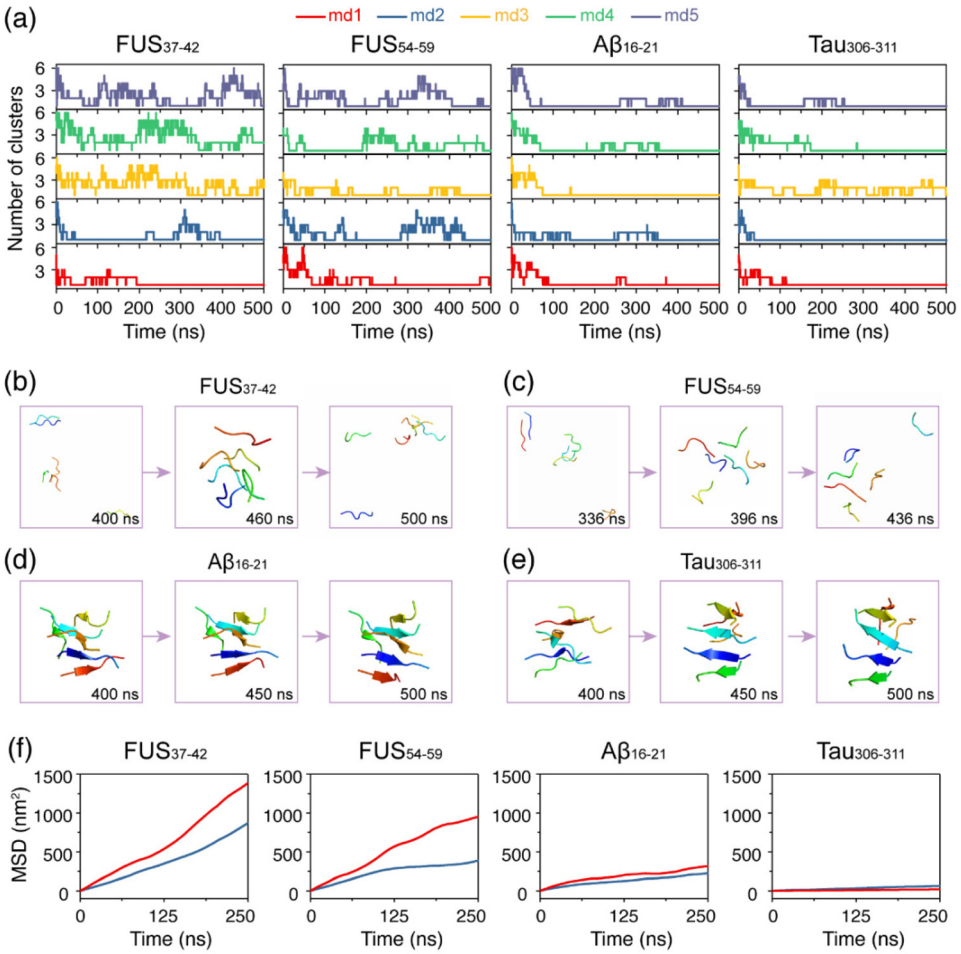

Fig. 2 The self-assembly properties of the $FUS_{37–42}$, $FUS_{54–59}$, $A\beta_{16–21}$ and $Tau_{306–311}$ hexapeptides into oligomers. (a) Time evolution of the number of clusters formed by each peptide at 310 K. (b–e) Snapshots of the representative states in one out of the five simulations for each system. Peptides were drawn in cartoon form using PyMOL with different chains in different colors. (f) Mean square displacement (MSD) of the four systems at 310 and 340 K. The MD simulations at 340 K started from the final states obtained at 310 K.

into stable aggregates, reflecting the irreversibility of their self-assembly processes. Additionally, side chain dihedral transition rates were also examined. Much higher transition rates were observed for $FUS_{37–42}$ and $FUS_{54–59}$ than for the $A\beta_{16–21}$ and $Tau_{306–311}$ oligomers, indicative of the higher side chain dynamics of the LARKS peptides (Fig. S4†). The different self-assembly dynamics were also demonstrated in the representative states of the four systems shown in Fig. 2b–e.

To further explore the thermostability of the oligomers formed at 310 K, we performed a 500 ns MD simulation for each system at a higher temperature of 340 K starting from the final state obtained at 310 K. Fig. 2f shows that the slope of the mean square displacement (MSD) curves of $FUS_{37–42}$ and $FUS_{54–59}$ are both very large at 340 K and there is a big gap between the curves at 310 K and those at 340 K, suggesting strong temperature dependence of their fluidity. In sharp contrast, the MSD values of $A\beta_{16–21}$ and $Tau_{306–311}$ are quite similar at both temperatures, suggesting poor temperature dependence of their fluidity. Moreover, $A\beta_{16–21}$ and $Tau_{306–311}$ have much smaller MSD values than $FUS_{37–42}$ and $FUS_{54–59}$, indicating their weaker mobility at both temperatures. Overall, the LARK segments $FUS_{37–42}$ and $FUS_{54–59}$ self-assemble into dynamic aggregates with high mobility and low thermal stability, while $A\beta_{16–21}$ and $Tau_{306–311}$ self-assemble into more stable aggregates.

Peptide chains in the $FUS_{37–42}$ and $FUS_{54–59}$ oligomers tend to be kinked with low β-sheet contents, while those in the $A\beta_{16–21}$ and $Tau_{306–311}$ oligomers are extended with high β-sheet contents

We further analyzed the structural features of the oligomers formed by each of the four peptides. Fig. 3a and b shows the probability density function (PDF) of the end-to-end distance of all the peptide chains in each system. It can be seen that the end-to-end distance distribution curves of the $FUS_{37–42}$ and $FUS_{54–59}$ peptides have two wide peaks, located at around 0.5 nm and 1.4 nm (Fig. 3a), respectively, corresponding to the collapsed and extended single-chain conformations (illustrated

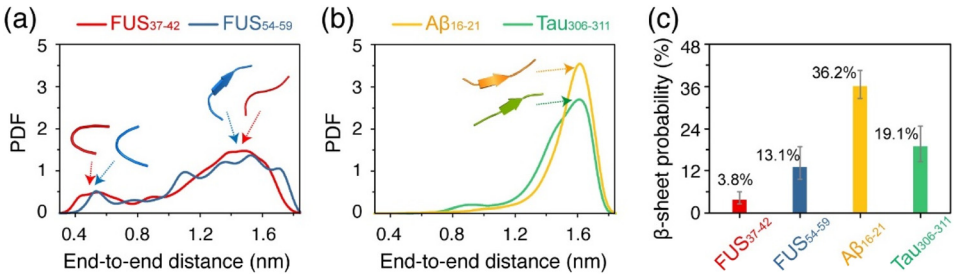

Fig. 3 The structural properties of the oligomers formed by each of the four different peptides. Probability density function (PDF) of the distance between the first and the last Cα atoms of all single chains in (a) the $FUS_{37–42}$ and $FUS_{54–59}$ systems and (b) the $Aβ_{16–21}$ and $Tau_{306–311}$ systems. Arrows in (a) and (b) show the extended/kinked and extended single chain conformations. (c) β-sheet probability of the four systems. Data are from 300 to 500 ns. The error bars were calculated using a bootstrap procedure of 50 resamplings, with a confidence interval of 10%.

by the representative snapshots in the dashed boxes). In contrast, the curves of the $Aβ_{16–21}$ and $Tau_{306–311}$ peptides have only one peak at around 1.6 nm (Fig. 3b). The results suggest that the peptide chains in the $FUS_{37–42}$/$FUS_{54–59}$ oligomers adopted both extended and collapsed conformations, whereas those in the $Aβ_{16–21}$/$Tau_{306–311}$ oligomers had mostly extended conformations. Moreover, the $FUS_{37–42}$/$FUS_{54–59}$ chains (with an end-to-end distance of 1.4 nm) were less extended than the $Aβ_{16–21}$/$Tau_{306–311}$ chains (1.6 nm), indicative of the kinked conformations of $FUS_{37–42}$/$FUS_{54–59}$ peptides. Collapsed peptides were likely to form more intra-molecular interactions, while extended peptides tended to form more inter-molecular interactions. Therefore, the peak at 0.5/1.4 nm of the distance distribution curves of the $FUS_{37–42}$ and $FUS_{54–59}$ systems signified that the collapsed/kinked peptides were less likely to form stable inter-molecular interactions, which may disfavor the formation of stable cross-β structures.

The β-sheet probability of the peptides in the four systems was calculated and is shown in Fig. 3c. The four systems with β-sheet contents from high to low are: $Aβ_{16–21}$ (36.2%), $Tau_{306–311}$ (19.1%), $FUS_{54–59}$ (13.1%) and $FUS_{37–42}$ (3.8%). Intriguingly, the $FUS_{37–42}$ (SYSGYS) oligomers had much lower β-sheet content than the $FUS_{54–59}$ (SYSSYG) oligomers, although the two peptides had the same amino acid composition (see below for a more detailed discussion). These results demonstrate that both $Aβ_{16–21}$ and $Tau_{306–311}$ peptides had a higher propensity to form β-sheet structures than the $FUS_{37–42}$ and $FUS_{54–59}$ peptides. Considering that β-sheets form the spines of stable amyloid fibrils, the different β-sheet preferences of the $FUS_{37–42}$/$FUS_{54–59}$ and $Aβ_{16–21}$/$Tau_{306–311}$ peptides may lead to their reversible and irreversible self-assembly.

The alternating stickers and spacers in the $FUS_{37–42}$/$FUS_{54–59}$ peptides result in the formation of reversible aggregates, while hydrophobic patches in the $Aβ_{16–21}$/$Tau_{306–311}$ peptides are responsible for their irreversible self-assembly

After examining the reversible and irreversible self-assembly properties of the two types of peptides, we further explored the underlying driving forces by calculating the number of inter-molecular contacts and H-bonds (Fig. 4). There were similar numbers of contacts between the main chains (MC–MC) among the four systems, while the contacts between the side chains (SC–SC) were considerably different, *i.e.* much higher in the $Aβ_{16–21}$ and $Tau_{306–311}$ systems than in the $FUS_{37–42}$ and $FUS_{54–59}$ systems (Fig. 4a). These results indicate that the SC–SC contacts in the four systems were the main interactions driving the reversible and irreversible self-assembly of the $FUS_{37–42}$/$FUS_{54–59}$ and $Aβ_{16–21}$/$Tau_{306–311}$ peptides. In addition, more MC–MC H-bonds were formed in the $FUS_{54–59}$, $Aβ_{16–21}$ and $Tau_{306–311}$ systems than in the $FUS_{37–42}$ system (Fig. 4b), consistent with the results of the formation of more β-sheets in the former three systems. Fig. 4b also shows that the SC–SC H-bonds only accounted for a minor part of the forces driving the peptide self-assembly in all the systems. Moreover, the numbers of H-bonds formed were different in the $FUS_{37–42}$ and $FUS_{54–59}$ oligomers. Although having the same amino acid compositions and containing the tandem SYS and SYG/GYS motifs, $FUS_{54–59}$ (SYSSYG) with Ser in the middle of the sequence had a greater ability to form intermolecular H-bonds than $FUS_{37–42}$ (SYSGYS) with Gly in the middle of the sequence, indicating that the Ser residue at middle positions had more significant influences on peptide self-assembly than the Gly residue and that the site-specific patterning of the spacer residues (Ser and Gly) can subtly tune the self-assembly behavior.

We note that there is an increase in the average contact number for the $Aβ_{16–21}$ systems starting from ~300 ns. To examine whether the contact number further rises with the increase of simulation time, we extended all five $Aβ_{16–21}$ oligomer simulations for an additional 150 ns and calculated the time evolution of their main chain and side chain contact numbers (Fig. S6†). For some simulations, the contact numbers remained mostly constant after 500 ns (such as the main chain contact for MD3 and the side chain contact for MD5). For most simulations, the contact numbers fluctuated around their equilibrium values. Importantly, trends of continued growth were not observed after 500 ns, suggesting that the 500 ns duration was sufficient to reach a convergence for these contact numbers.

The intermolecular MC–MC and SC–SC residue-wise contacts and H-bonds were also analyzed (Fig. 4c, d and S7, S8†). As seen from Fig. 4c, only Tyr residues, separated by Ser and Gly, had strong interactions with each other in the $FUS_{37–42}$ and $FUS_{54–59}$ systems, suggesting that Tyr residues are crucial

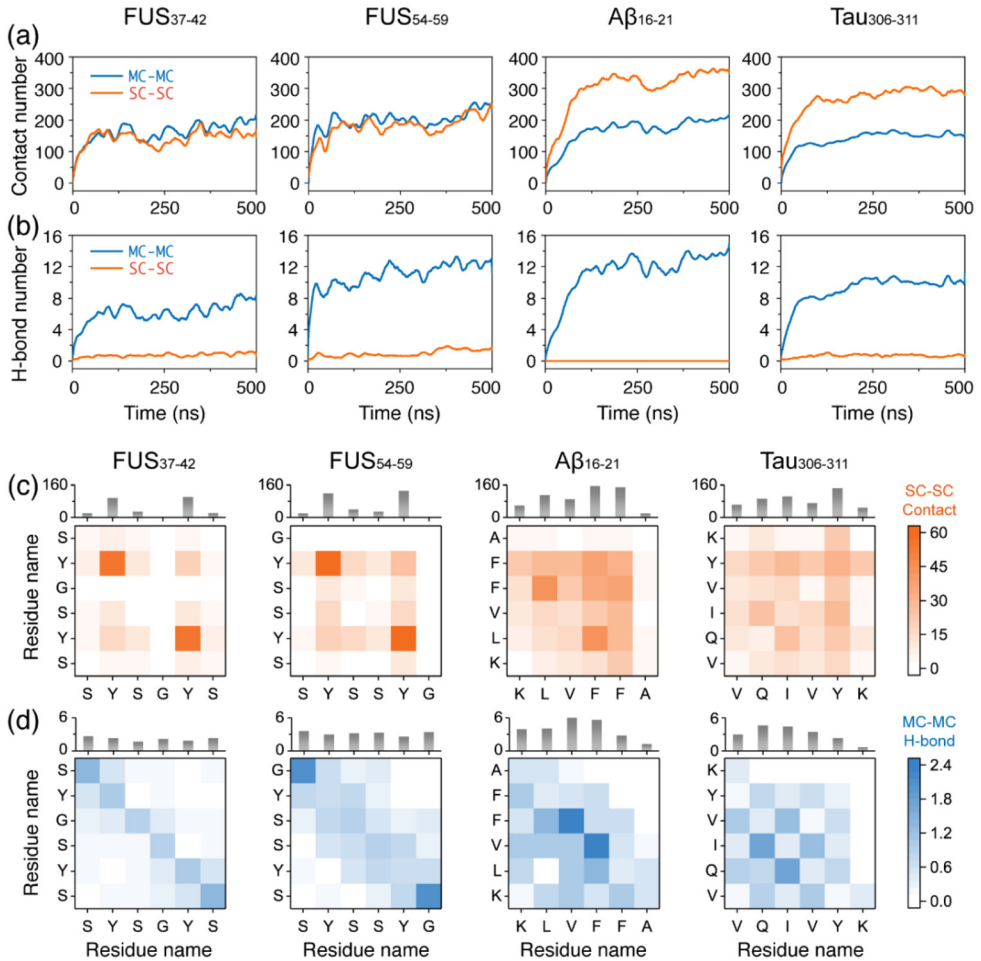

Fig. 4 The driving forces underlying the reversible self-assembly of the FUS_{37-42}/FUS_{54-59} peptides and irreversible self-assembly of the $A\beta_{16-21}$ and $Tau_{306-311}$ peptides. Time evolution of (a) main chain–main chain (MC–MC) and side chain–side chain (SC–SC) contacts, as well as (b) MC–MC and SC–SC H-bonds in the FUS_{37-42}, FUS_{54-59}, $A\beta_{16-21}$ and $Tau_{306-311}$ systems. Inter-molecular residue-wise (c) SC–SC contacts and (d) MC–MC H-bonds of the four systems. The grey bar charts show the cumulative contact numbers between each residue and other residues.

stickers of FUS_{37-42} and FUS_{54-59}. The important role of Tyr and repeated motifs containing Tyr in contributing to protein LLPS has been reported in many studies.[73–75] The amphipathic side chain of Tyr allowed it to form a hydrogen bond *via* its phenol group, as well as π–π interaction through the aromatic ring, the latter of which is important for the assembly of various amyloid peptides into β-rich fibrils,[76,77] and has emerged as a major driver of LLPS.[78–80] The intermolecular π–π stacking interactions were calculated between aromatic rings in the four systems. It is shown in Fig. S9† that more π–π stacking interactions were formed in the FUS_{37-42} and FUS_{54-59} systems than in the $A\beta_{16-21}$ and $Tau_{306-311}$ systems, although the number of aromatic rings was the same in FUS_{37-42}, FUS_{54-59} (containing two Tyr residues) and $A\beta_{16-21}$ (containing two Phe residues). The distribution patterns of the π stacking angle were alike in the four all-atom oligomer systems, mainly preferring perpendicular stacking, except for FUS_{54-59} with an equal preference for T-shape stacking. Although with strong SC–SC interactions *via* π–π stacking, H-bonding and hydrophobic interactions between Tyr residues, the occurrence of the polar spacers of Ser and Gly impeded the formation of successive strong interactions in the FUS_{37-42} and FUS_{54-59} systems, but enabled transient intermolecular interactions favorable for LLPS. The sticker–spacer architecture is ubiquitous in LLPS-prone proteins[81] and the sticker–sticker, spacer–spacer and sticker–spacer interactions interplay[82] during their LLPS process. FUS_{37-42} and FUS_{54-59} peptides possess alternating stickers (Tyr) and spacers (Ser and Gly), and the transient interactions among stickers and spacers may facilitate the reversible self-assembly. In contrast, the central consecutive hydrophobic residues LVFF in $A\beta_{16-21}$ and IVY in $Tau_{306-311}$, acting as hydrophobic patches, have higher contact numbers with all residues through side chain contacts. The hydrophobic patch provides persistent interactions, contributing to peptide irreversible self-assembly. Additionally, the correlations between side chain and main chain dynamics were examined by calculating the Pearson correlation coefficients between main chain dihedrals ϕ/ψ and side chain dihedral χ_1. Our calculations suggest a low main chain–side chain correlation, with correlation coefficients <0.3 (Fig. S10 and S11†). These

results further demonstrate that main chain and side chain play different roles in the assembly process.

The role of water in the self-assembly process of these peptides was examined by calculating the number of hydrogen bonds (H-bonds) formed between the side chain of each residue and water molecules (Fig. S12†). The results suggest that the FUS_{37-42}/FUS_{54-59} peptides formed much more H-bonds with water through five out of six residues (Ser and Tyr). In contrast, only three residues (Gln, Tyr, and Lys) in the $Tau_{306-311}$ peptides, and only one residue (Lys) in the $A\beta_{16-21}$ peptide formed side chain H-bonds with water. These results are consistent with the lower assembly capability and the higher fluidity of FUS_{37-42}/FUS_{54-59} condensates than $A\beta_{16-21}$/$Tau_{306-311}$ aggregates, and demonstrate the importance of water in the reversible/irreversible assembly process. A previous MD study[83] has reported that the interaction of water plays an important role in the fibrillization of the Gln-containing polar heptapeptide, GNNQQNY, from the prion domain of Sup35. Interestingly, among all residues in the four peptides, the glutamine residue in the $Tau_{306-311}$ peptide formed the highest number of H-bonds with water molecules, suggesting its role in mediating the assembly of $Tau_{306-311}$.

Taken together, the aromatic sticker residue (Tyr) in the LARK segments, FUS_{37-42} (SYSGYS) and FUS_{54-59} (SYSSYG), are separated by spacer residues (Ser and Gly). The alternating stickers and spacers cause FUS_{37-42} and FUS_{54-59} to self-assemble into reversible aggregates. In contrast, the side chain interactions between the hydrophobic patches cause irreversible self-assembly of the $A\beta_{16-21}$ and $Tau_{306-311}$ peptides. These two peptides self-assemble into aggregates with high β-sheets. Side chain hydrophobic interactions and main chain H-bonding interactions collectively stabilize the aggregates (Fig. 4c and d).

FUS_{37-42}, FUS_{54-59}, $A\beta_{16-21}$ and $Tau_{306-311}$ present distinct phase separation propensities

An increasing number of studies have demonstrated that LLPS is a general property of peptides and proteins,[18,19,25] and even

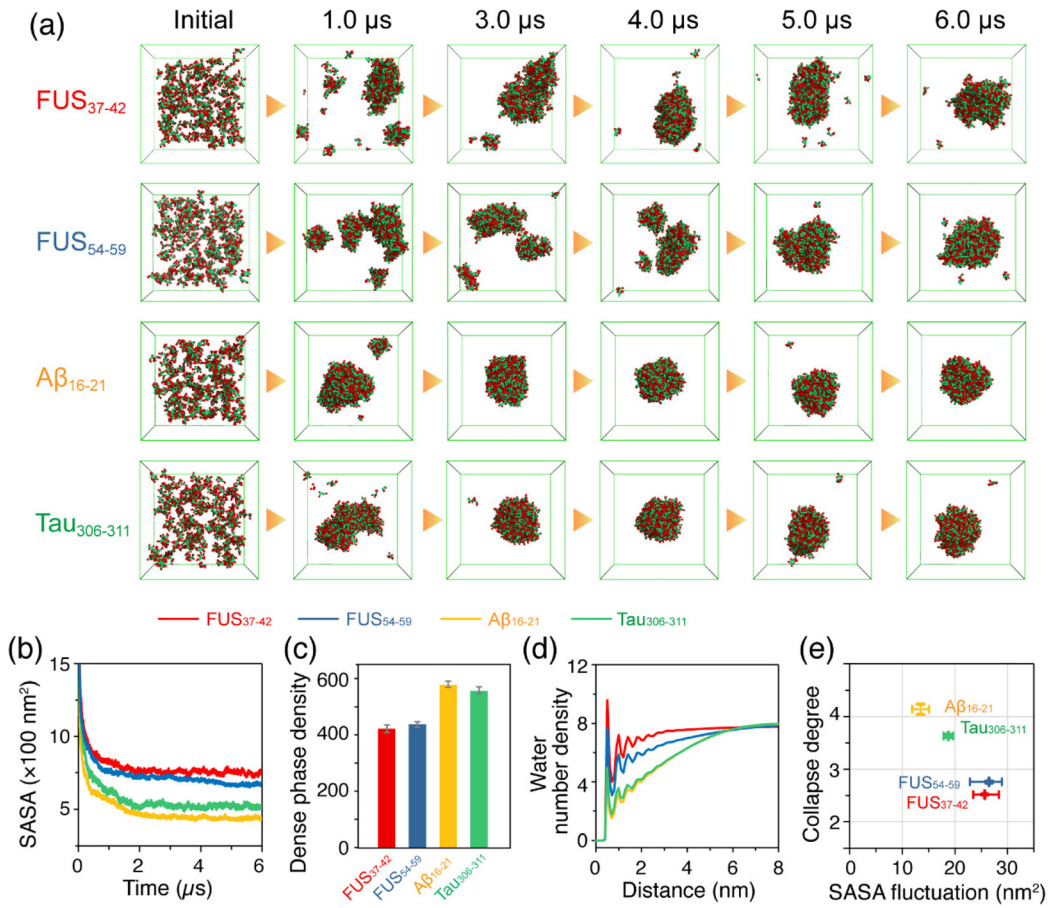

Fig. 5 Phase separation behaviors of the FUS_{37-42}, FUS_{54-59}, $A\beta_{16-21}$ and $Tau_{306-311}$ hexapeptides predicted by multiple microsecond CG-MD simulations. (a) Representative snapshots of each system at six time points in 6 μs CG-MD simulations. (b) Time evolution of SASA of the FUS_{37-42}, FUS_{54-59}, $A\beta_{16-21}$ and $Tau_{306-311}$ peptides. Values were averaged over three independent 6 μs MD simulations for each system. (c) Concentrations of the dense phase of the four systems. (d) Number density of water molecules as a function of distance from the center of the condensed phase in the four systems. (e) The collapse degree values and the fluctuation of SASA of the four systems. Detailed descriptions of the parameters used are listed in the Models and Methods section.

short peptides possess sufficient interaction sites for LLPS.[42,43] In order to predict the phase separation propensity of the hexapeptides, we carried out CG-MD simulations on large space and time scales based on a modified MARTINI-2.2 force field with a down-scaling of the van der Waals parameters between Ser pseudo-atoms and the backbone beads of all the amino acid residues in the $FUS_{37–42}$ and $FUS_{54–59}$ systems.[54,55] Three individual 6 μs CG-MD simulations were carried out for each of the hexapeptide systems: $FUS_{37–42}$, $FUS_{54–59}$, $Aβ_{16–21}$ and $Tau_{306–311}$, starting from the initial states with 200 monomers randomly dispersed in the box. A detailed description of the scaling method is given in the Models and Methods section. The representative snapshots of the four hexapeptide systems in Fig. 5a show that $FUS_{37–42}$, $FUS_{54–59}$, $Tau_{306–311}$ and $Aβ_{16–21}$ were all able to self-assemble into a dense phase with ascending phase separation capabilities qualitatively consistent with the self-assembly propensity in the AA-MD simulations of the oligomer systems. Specifically, the $FUS_{37–42}$ and $FUS_{54–59}$ condensates exhibited a loosely packed feature and were highly dynamic. In contrast, $Aβ_{16–21}$ and $Tau_{306–311}$ condensates were more compact and remained relatively stable in shape as the simulation time increased. The $FUS_{37–42}$ and $FUS_{54–59}$ aggregates had a larger solvent accessible surface area (SASA) than the $Aβ_{16–21}$ and $Tau_{306–311}$ aggregates (Fig. 5b), suggesting lower phase separation propensities. The concentrations of the $FUS_{37–42}$ and $FUS_{54–59}$ dense phases were lower than those of the $Aβ_{16–21}$ and $Tau_{306–311}$ dense phases (Fig. 5c). These results indicate that the assemblies formed by the $Aβ_{16–21}$ and $Tau_{306–311}$ peptides were probably hydrogel-like with a high degree of solvent exclusion, and $FUS_{37–42}$ and $FUS_{54–59}$ assemblies were more like liquid droplets containing water molecules (Fig. 5d, larger number density of water molecules). Additionally, the cross-sections of the assemblies formed by the four peptides were provided to further demonstrate the presence of water molecules in the condensates. It can be seen from Fig. S13† that the $FUS_{34–42}$ and $FUS_{54–59}$ assemblies were embedded with water molecules. These water molecules may have contributed to their fluidities and also played a role in stabilizing the $FUS_{37–42}/FUS_{54–59}$ condensates. In contrast, the $Aβ_{16–21}$ and $Tau_{306–311}$ assemblies were densely packed and solid-like. Therefore, we infer that the LARK segments $FUS_{37–42}$ and $FUS_{54–59}$ underwent LLPS, and the $Aβ_{16–21}$ and $Tau_{306–311}$ peptides underwent LSPS. To more quantitatively characterize the different properties of the phase separations of the four peptides, we selected two order parameters, namely the collapse degree and the fluctuation of SASA (Fig. 5e), to manifest the phase separation propensities and the liquidity of the dense phase, respectively. It is shown that the aggregates formed by the $Aβ_{16–21}$ and $Tau_{306–311}$ peptides have a larger collapse degree and smaller SASA fluctuation, while those formed by the $FUS_{37–42}$ and $FUS_{54–59}$ peptides have a smaller collapse degree and larger SASA fluctuation, indicative of the higher fluidity of the $FUS_{37–42}/FUS_{54–59}$ aggregates.

Collectively, our CG-MD simulations suggest that the LARK segments $FUS_{37–42}$ and $FUS_{54–59}$ have low phase separation propensities and their condensates are highly dynamic and loosely packed with high mobility. In contrast, the $Aβ_{16–21}$ and $Tau_{306–311}$ peptides have high phase separation propensities and the aggregates are more like solids with low degrees of liquidity. Therefore, we postulate that $FUS_{37–42}$ and $FUS_{54–59}$ undergo liquid–liquid phase separation, while $Aβ_{16–21}$ and $Tau_{306–311}$ peptides undergo liquid–solid phase separation.

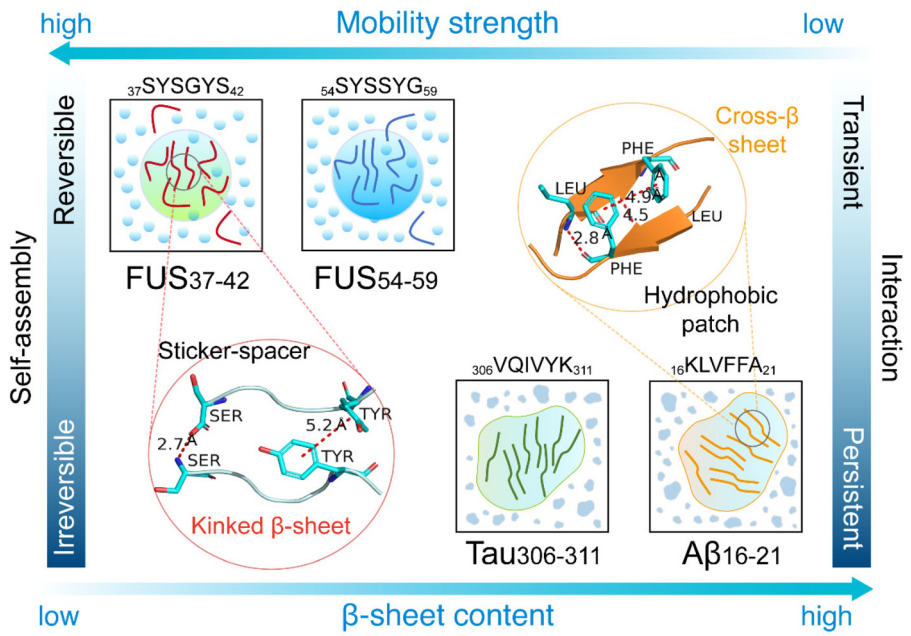

Fig. 6 Schematic diagram illustrating the reversible and irreversible self-assembly behaviors and mechanisms of the four hexapeptides.

Conclusions

In summary, we have investigated the reversible and irreversible self-assembly of four representative hexapeptides, $FUS_{37–42}$, $FUS_{54–59}$, $A\beta_{16–21}$ and $Tau_{306–311}$, by performing AA-MD and CG-MD simulations. We characterized the self-assembly dynamics of the four hexapeptides and predicted their LLPS/LSPS propensities. Our simulations showed that the four hexapeptides self-assembled into aggregates with different physical properties. The LARKS peptides, $FUS_{37–42}$ and $FUS_{54–59}$, formed coil-rich aggregates with high mobility and poor thermostability, while $A\beta_{16–21}$ and $Tau_{306–311}$ self-assembled into β-sheets with high thermostability. Interaction analyses indicated that the persistent interactions between the hydrophobic patches, namely LVFF in $A\beta_{16–21}$ and IVY in $Tau_{306–311}$, acted as the main forces driving the irreversible self-assembly of $A\beta_{16–21}$ and $Tau_{306–311}$ and maintaining the stability of the irreversible aggregates. In contrast, the alternating sticker (Tyr) and spacers (Ser and Gly) in the $FUS_{37–42}$ and $FUS_{54–59}$ peptides provided transient interactions, which were strong enough to drive reversible self-assembly or LLPS and yet weak enough to inhibit irreversible aggregation or LSPS. Intriguingly, the $FUS_{37–42}$ (SYSGYS) and $FUS_{54–59}$ (SYSSYG) peptides had the same sequence composition and the same number of sticker and spacer residues, but exhibited different self-assembly properties, suggesting that the site-specific patterning of spacer residues (Ser and Gly) had a non-negligible effect on peptide self-assembly behaviors. Fig. 6 offers a visual illustration of the varying assembly behaviors and mechanisms of these hexapeptide aggregates. Our current work reveals the molecular mechanisms of sequence-dependent reversible and irreversible self-assembly and the phase separation behaviors of short fibril-forming peptides from amyloid proteins and LLPS-prone proteins, paving the way for further in-depth understanding of reversible LLPS and irreversible aggregation of disease-related proteins including FUS, TDP-43, and tau proteins.

Author contributions

G. W., C. G., and Z. L. conceived the project and constructed the systems. Z. L. performed the all-atom simulations and analyzed the simulation data. Y. T. performed the coarse-grained simulations. G. W. and Z. L. drafted the manuscript. C. G. and G. W. edited the manuscript. All authors analyzed the data, and reviewed and approved the final version of the manuscript.

Conflicts of interest

There are no conflicts to declare.

Acknowledgements

This work is supported financially by the National Key Research and Development Program of China (Grant No. 2023YFF1204402), the National Natural Science Foundation of China (Grant No. 12074079, 11804218 and 12374208), the Natural Science Foundation of Shanghai (Grant No. 22ZR1406800), and the China Postdoctoral Science Foundation (Grant No. 2022M720815). All the MD simulations were performed using the GPU Cluster at Fudan University.

References

1 Y. S. Eisele, C. Monteiro, C. Fearns, S. E. Encalada, R. L. Wiseman, E. T. Powers and J. W. Kelly, Targeting protein aggregation for the treatment of degenerative diseases, *Nat. Rev. Drug Discovery*, 2015, **14**(11), 759–780.
2 F. Chiti and C. M. Dobson, Protein misfolding, amyloid formation, and human disease: a summary of progress over the last decade, *Annu. Rev. Biochem.*, 2017, **86**, 27–68.
3 D. J. Selkoe, Alzheimer's disease: genes, proteins, and therapy, *Physiol. Rev.*, 2001, **81**(2), 741–766.
4 F. M. LaFerla, K. N. Green and S. Oddo, Intracellular amyloid-beta in Alzheimer's disease, *Nat. Rev. Neurosci.*, 2007, **8**(7), 499–509.
5 U. Sengupta and R. Kayed, Amyloid beta, Tau, and alpha-Synuclein aggregates in the pathogenesis, prognosis, and therapeutics for neurodegenerative diseases, *Prog. Neurobiol.*, 2022, **214**, 102270.
6 D. S. Eisenberg and M. R. Sawaya, Structural studies of amyloid proteins at the molecular level, *Annu. Rev. Biochem.*, 2017, **86**, 69–95.
7 D. Li and C. Liu, Structural diversity of amyloid fibrils and advances in their structure determination, *Biochemistry*, 2020, **59**(5), 639–646.
8 N. El Mammeri, P. Duan, A. J. Dregni and M. Hong, Amyloid fibril structures of tau: Conformational plasticity of the second microtubule-binding repeat, *Sci. Adv.*, 2023, **9**(28), eadh4731.
9 N. Vettore and A. K. Buell, Thermodynamics of amyloid fibril formation from chemical depolymerization, *Phys. Chem. Chem. Phys.*, 2019, **21**(47), 26184–26194.
10 B. Morel, L. Varela and F. Conejero-Lara, The thermodynamic stability of amyloid fibrils studied by differential scanning calorimetry, *J. Phys. Chem. B*, 2010, **114**(11), 4010–4019.
11 D. T. Murray, M. Kato, Y. Lin, K. R. Thurber, I. Hung, S. L. McKnight and R. Tycko, Structure of FUS protein fibrils and its relevance to self-assembly and phase separation of low-complexity domains, *Cell*, 2017, **171**(3), 615–627.
12 F. Luo, X. Gui, H. Zhou, J. Gu, Y. Li, X. Liu, M. Zhao, D. Li, X. Li and C. Liu, Atomic structures of FUS LC domain segments reveal bases for reversible amyloid fibril formation, *Nat. Struct. Mol. Biol.*, 2018, **25**(4), 341–346.
13 M. P. Hughes, M. R. Sawaya, D. R. Boyer, L. Goldschmidt, J. A. Rodriguez, D. Cascio, L. Chong, T. Gonen and D. S. Eisenberg, Atomic structures of low-complexity protein segments reveal kinked beta sheets that assemble networks, *Science*, 2018, **359**(6376), 698–701.

14 Q. Cao, D. R. Boyer, M. R. Sawaya, P. Ge and D. S. Eisenberg, Cryo-EM structures of four polymorphic TDP-43 amyloid cores, *Nat. Struct. Mol. Biol.*, 2019, **26**(7), 619–627.
15 E. L. Guenther, Q. Cao, H. Trinh, J. Lu, M. R. Sawaya, D. Cascio, D. R. Boyer, J. A. Rodriguez, M. P. Hughes and D. S. Eisenberg, Atomic structures of TDP-43 LCD segments and insights into reversible or pathogenic aggregation, *Nat. Struct. Mol. Biol.*, 2018, **25**(6), 463–471.
16 X. Gui, F. Luo, Y. Li, H. Zhou, Z. Qin, Z. Liu, J. Gu, M. Xie, K. Zhao, B. Dai, *et al.*, Structural basis for reversible amyloids of hnRNPA1 elucidates their role in stress granule assembly, *Nat. Commun.*, 2019, **10**(1), 2006–2017.
17 K. A. Murray, D. Evans, M. P. Hughes, M. R. Sawaya, C. J. Hu, K. N. Houk and D. Eisenberg, Extended beta-Strands Contribute to Reversible Amyloid Formation, *ACS Nano*, 2022, **16**(2), 2154–2163.
18 M. Hardenberg, A. Horvath, V. Ambrus, M. Fuxreiter and M. Vendruscolo, Widespread occurrence of the droplet state of proteins in the human proteome, *Proc. Natl. Acad. Sci. U. S. A.*, 2020, **117**(52), 33254–33262.
19 M. Poudyal, K. Patel, L. Gadhe, A. S. Sawner, P. Kadu, D. Datta, S. Mukherjee, S. Ray, A. Navalkar, S. Maiti, *et al.*, Intermolecular interactions underlie protein/peptide phase separation irrespective of sequence and structure at crowded milieu, *Nat. Commun.*, 2023, **14**(1), 6199.
20 A. Molliex, J. Temirov, J. Lee, M. Coughlin, A. P. Kanagaraj, H. J. Kim, T. Mittag and J. P. Taylor, Phase separation by low complexity domains promotes stress granule assembly and drives pathological fibrillization, *Cell*, 2015, **163**(1), 123–133.
21 L. Guo and J. Shorter, It's raining liquids: RNA tunes viscoelasticity and dynamics of membraneless organelles, *Mol. Cell*, 2015, **60**(2), 189–192.
22 S. Saha, C. A. Weber, M. Nousch, O. Adame-Arana, C. Hoege, M. Y. Hein, E. Osborne-Nishimura, J. Mahamid, M. Jahnel, L. Jawerth, *et al.*, Polar positioning of phase-separated liquid compartments in cells regulated by an mRNA competition mechanism, *Cell*, 2016, **166**(6), 1572–1584.
23 S. Boeynaems, S. Alberti, N. L. Fawzi, T. Mittag, M. Polymenidou, F. Rousseau, J. Schymkowitz, J. Shorter, B. Wolozin, L. Van Den Bosch, *et al.*, Protein Phase Separation: A New Phase in Cell Biology, *Trends Cell Biol.*, 2018, **28**(6), 420–435.
24 Z. Wang and H. Zhang, Phase separation, transition, and autophagic degradation of proteins in development and pathogenesis, *Trends Cell Biol.*, 2019, **29**(5), 417–427.
25 S. Maharana, J. Wang, D. K. Papadopoulos, D. Richter, A. Pozniakovsky, I. Poser, M. Bickle, S. Rizk, J. Guillen-Boixet, T. M. Franzmann, *et al.*, RNA buffers the phase separation behavior of prion-like RNA binding proteins, *Science*, 2018, **360**(6391), 918–921.
26 Y. Shin and C. P. Brangwynne, Liquid phase condensation in cell physiology and disease, *Science*, 2017, **357**(6357), eaaf4382.
27 S. Alberti, A. Gladfelter and T. Mittag, Considerations and Challenges in Studying Liquid-Liquid Phase Separation and Biomolecular Condensates, *Cell*, 2019, **176**(3), 419–434.
28 H. Yoo, C. Triandafillou and D. A. Drummond, Cellular sensing by phase separation: using the process, not just the products, *J. Biol. Chem.*, 2019, **294**(18), 7151–7159.
29 J. G. Daigle, N. A. Lanson Jr., R. B. Smith, I. Casci, A. Maltare, J. Monaghan, C. D. Nichols, D. Kryndushkin, F. Shewmaker and U. B. Pandey, RNA-binding ability of FUS regulates neurodegeneration, cytoplasmic mislocalization and incorporation into stress granules associated with FUS carrying ALS-linked mutations, *Hum. Mol. Genet.*, 2013, **22**(6), 1193–1205.
30 A. Patel, H. O. Lee, L. Jawerth, S. Maharana, M. Jahnel, M. Y. Hein, S. Stoynov, J. Mahamid, S. Saha, T. M. Franzmann, *et al.*, A liquid-to-solid phase transition of the ALS protein FUS accelerated by disease mutation, *Cell*, 2015, **162**(5), 1066–1077.
31 J. P. Taylor, R. H. Brown Jr. and D. W. Cleveland, Decoding ALS: from genes to mechanism, *Nature*, 2016, **539**(7628), 197–206.
32 G. Antonacci, V. de Turris, A. Rosa and G. Ruocco, Background-deflection Brillouin microscopy reveals altered biomechanics of intracellular stress granules by ALS protein FUS, *Commun. Biol.*, 2018, **1**, 139.
33 A. G. Niaki, J. Sarkar, X. Cai, K. Rhine, V. Vidaurre, B. Guy, M. Hurst, J. C. Lee, H. R. Koh, L. Guo, *et al.*, Loss of dynamic RNA interaction and aberrant phase separation induced by two distinct types of ALS/FTD-linked FUS mutations, *Mol. Cell*, 2020, **77**(1), 82–94.
34 E. Bogaert, S. Boeynaems, M. Kato, L. Guo, T. R. Caulfield, J. Steyaert, W. Scheveneels, N. Wilmans, W. Haeck, N. Hersmus, *et al.*, Molecular Dissection of FUS Points at Synergistic Effect of Low-Complexity Domains in Toxicity, *Cell Rep.*, 2018, **24**(3), 529–537.
35 S. Qamar, G. Wang, S. J. Randle, F. S. Ruggeri, J. A. Varela, J. Q. Lin, E. C. Phillips, A. Miyashita, D. Williams, F. Strohl, *et al.*, FUS phase separation is modulated by a molecular chaperone and methylation of arginine cation-pi interactions, *Cell*, 2018, **173**(3), 720–734.
36 C. Chen, X. Ding, N. Akram, S. Xue and S. Z. Luo, Fused in sarcoma: properties, self-assembly and correlation with neurodegenerative diseases, *Molecules*, 2019, **24**(8), 1622–1638.
37 S. Li, T. Yoshizawa, Y. Shiramasa, M. Kanamaru, F. Ide, K. Kitamura, N. Kashiwagi, N. Sasahara, S. Kitazawa and R. Kitahara, Mechanism underlying liquid-to-solid phase transition in fused in sarcoma liquid droplets, *Phys. Chem. Chem. Phys.*, 2022, **24**(32), 19346–19353.
38 D. T. Murray and R. Tycko, Side Chain Hydrogen-Bonding Interactions within Amyloid-like Fibrils Formed by the Low-Complexity Domain of FUS: Evidence from Solid State Nuclear Magnetic Resonance Spectroscopy, *Biochemistry*, 2020, **59**(4), 364–378.

39 W. M. Babinchak and W. K. Surewicz, Liquid-Liquid Phase Separation and Its Mechanistic Role in Pathological Protein Aggregation, *J. Mol. Biol.*, 2020, **432**(7), 1910–1925.
40 D. De Sancho, Phase, separation in amino acid mixtures is governed by composition, *Biophys. J.*, 2022, **121**(21), 4119–4127.
41 G. Valdes-Garcia, K. Gamage, C. Smith, K. Martirosova, M. Feig and L. J. Lapidus, The effect of polymer length in liquid-liquid phase separation, *Cell Rep. Phys. Sci.*, 2023, **4**(5), 101415.
42 M. Abbas, W. P. Lipiński, K. K. Nakashima, W. T. Huck and E. Spruijt, A short peptide synthon for liquid–liquid phase separation, *Nat. Chem.*, 2021, **13**(11), 1046–1054.
43 Y. Tang, S. Bera, Y. Yao, J. Zeng, Z. Lao, X. Dong, E. Gazit and G. Wei, Prediction and characterization of liquid-liquid phase separation of minimalistic peptides, *Cell Rep. Phys. Sci.*, 2021, **2**(9), 100579–100596.
44 J. P. Colletier, A. Laganowsky, M. Landau, M. Zhao, A. B. Soriaga, L. Goldschmidt, D. Flot, D. Cascio, M. R. Sawaya and D. Eisenberg, Molecular basis for amyloid-beta polymorphism, *Proc. Natl. Acad. Sci. U. S. A.*, 2011, **108**(41), 16938–16943.
45 M. R. Sawaya, S. Sambashivan, R. Nelson, M. I. Ivanova, S. A. Sievers, M. I. Apostol, M. J. Thompson, M. Balbirnie, J. J. Wiltzius, H. T. McFarlane, *et al.*, Atomic structures of amyloid cross-beta spines reveal varied steric zippers, *Nature*, 2007, **447**(7143), 453–457.
46 *The PyMOL molecular graphics system, Version 1.8*, 2015.
47 M. J. Abraham, T. Murtola, R. Schulz, S. Páll, J. C. Smith, B. Hess and E. Lindahl, GROMACS: high performance molecular simulations through multi-level parallelism from laptops to supercomputers, *SoftwareX*, 2015, **1–2**, 19–25.
48 K. Lindorff-Larsen, S. Piana, K. Palmo, P. Maragakis, J. L. Klepeis, R. O. Dror and D. E. Shaw, Improved side-chain torsion potentials for the Amber ff99SB protein force field, *Proteins*, 2010, **78**(8), 1950–1958.
49 M. Deserno and C. Holm, How to mesh up Ewald sums. I. A theoretical and numerical comparison of various particle mesh routines, *J. Chem. Phys.*, 1998, **109**(18), 7678–7693.
50 M. Deserno and C. Holm, How to mesh up Ewald sums. II. An accurate error estimate for the particle-particle-particle-mesh algorithm, *J. Chem. Phys.*, 1998, **109**(18), 7694–7701.
51 X. Liu, Z. Lao, X. Li, X. Dong and G. Wei, ALS-associated A315E and A315pT variants exhibit distinct mechanisms in inducing irreversible aggregation of TDP-43 312-317 peptide, *Phys. Chem. Chem. Phys.*, 2022, **24**(26), 16263–16273.
52 G. Bussi, D. Donadio and M. Parrinello, Canonical sampling through velocity rescaling, *J. Chem. Phys.*, 2007, **126**(1), 014101.
53 M. Parrinello and A. Rahman, Polymorphic transitions in single-crystals - a new molecular-dynamics method, *J. Appl. Phys.*, 1981, **52**(12), 7182–7190.
54 D. H. de Jong, G. Singh, W. F. Bennett, C. Arnarez, T. A. Wassenaar, L. V. Schafer, X. Periole, D. P. Tieleman and S. J. Marrink, Improved parameters for the MARTINI coarse-grained protein force field, *J. Chem. Theory Comput.*, 2013, **9**(1), 687–697.
55 A. C. Stark, C. T. Andrews and A. H. Elcock, Toward optimized potential functions for protein-protein interactions in aqueous solutions: osmotic second virial coefficient calculations using the MARTINI coarse-grained force field, *J. Chem. Theory Comput.*, 2013, **9**(9), 4176–4185.
56 I. G. Tironi, R. Sperb, P. E. Smith and W. F. Vangunsteren, A generalized reaction field method for molecular-dynamics simulations, *J. Chem. Phys.*, 1995, **102**(13), 5451–5459.
57 A. C. Stark, C. T. Andrews and A. H. Elcock, Toward optimized potential functions for protein-protein interactions in aqueous solutions: osmotic second virial coefficient calculations using the MARTINI coarse-grained force field, *J. Chem. Theory Comput.*, 2013, **9**(9), 4176–4185.
58 Z. Benayad, S. von Bulow, L. S. Stelzl and G. Hummer, Simulation of FUS Protein Condensates with an Adapted Coarse-Grained Model, *J. Chem. Theory Comput.*, 2021, **17**(1), 525–537.
59 Y. Tang, S. Bera, Y. Yao, J. Zeng, Z. Lao, X. Dong, E. Gazit and G. Wei, Prediction and characterization of liquid-liquid phase separation of minimalistic peptides, *Cell Rep. Phys. Sci.*, 2021, **2**(9), 100579.
60 A. Huet and P. Derreumaux, Impact of the mutation A21G (Flemish variant) on Alzheimer's beta-amyloid dimers by molecular dynamics simulations, *Biophys. J.*, 2006, **91**(10), 3829–3840.
61 Y. Luo, B. Ma, R. Nussinov and G. Wei, Structural Insight into Tau Protein's Paradox of Intrinsically Disordered Behavior, Self-Acetylation Activity, and Aggregation, *J. Phys. Chem. Lett.*, 2014, **5**(17), 3026–3031.
62 Z. Lao, Y. Chen, Y. Tang and G. Wei, Molecular dynamics simulations reveal the inhibitory mechanism of dopamine against human islet amyloid polypeptide (hIAPP) aggregation and its destabilization effect on hIAPP protofibrils, *ACS Chem. Neurosci.*, 2019, **10**(9), 4151–4159.
63 R. B. Fenwick, L. Orellana, S. Esteban-Martin, M. Orozco and X. Salvatella, Correlated motions are a fundamental property of beta-sheets, *Nat. Commun.*, 2014, **5**, 4070.
64 S. R. Jammalamadaka and A. SenGupta, *Topics in circular statistics*, world scientific, 2001.
65 H. Li, Y. Luo, P. Derreumaux and G. Wei, Carbon nanotube inhibits the formation of beta-sheet-rich oligomers of the Alzheimer's amyloid-beta(16-22) peptide, *Biophys. J.*, 2011, **101**(9), 2267–2276.
66 P. H. Nguyen, J. M. Campanera, S. T. Ngo, A. Loquet and P. Derreumaux, Tetrameric Abeta40 and Abeta42 beta-Barrel Structures by Extensive Atomistic Simulations. II. In Aqueous Solution, *J. Phys. Chem. B*, 2019, **123**(31), 6750–6756.
67 V. H. Man, X. He, J. Gao and J. Wang, Effects of All-Atom Molecular Mechanics Force Fields on Amyloid Peptide Assembly: The Case of PHF6 Peptide of Tau Protein, *J. Chem. Theory Comput.*, 2021, **17**(10), 6458–6471.

68 W. G. Touw, C. Baakman, J. Black, T. A. te Beek, E. Krieger, R. P. Joosten and G. Vriend, A series of PDB-related databanks for everyday needs, *Nucleic Acids Res.*, 2015, **43**(D1), D364–D368.
69 S. K. Burley and G. A. Petsko, Aromatic-aromatic interaction: a mechanism of protein structure stabilization, *Science*, 1985, **229**(4708), 23–28.
70 P. W. Frederix, G. G. Scott, Y. M. Abul-Haija, D. Kalafatovic, C. G. Pappas, N. Javid, N. T. Hunt, R. V. Ulijn and T. Tuttle, Exploring the sequence space for (tri-)peptide self-assembly to design and discover new hydrogels, *Nat. Chem.*, 2015, **7**(1), 30–37.
71 W. Humphrey, A. Dalke and K. Schulten, VMD: visual molecular dynamics, *J. Mol. Graphics Modell.*, 1996, **14**(1), 33–38.
72 A. E. Aliev, M. Kulke, H. S. Khaneja, V. Chudasama, T. D. Sheppard and R. M. Lanigan, Motional timescale predictions by molecular dynamics simulations: case study using proline and hydroxyproline sidechain dynamics, *Proteins*, 2014, **82**(2), 195–215.
73 Y. Lin, S. L. Currie and M. K. Rosen, Intrinsically disordered sequences enable modulation of protein phase separation through distributed tyrosine motifs, *J. Biol. Chem.*, 2017, **292**(46), 19110–19120.
74 J. Wang, J. M. Choi, A. S. Holehouse, H. O. Lee, X. Zhang, M. Jahnel, S. Maharana, R. Lemaitre, A. Pozniakovsky, D. Drechsel, *et al.*, A molecular grammar governing the driving forces for phase separation of prion-like RNA binding proteins, *Cell*, 2018, **174**(3), 688–699.
75 A. C. Murthy, G. L. Dignon, Y. Kan, G. H. Zerze, S. H. Parekh, J. Mittal and N. L. Fawzi, Molecular interactions underlying liquid-liquid phase separation of the FUS low-complexity domain, *Nat. Struct. Mol. Biol.*, 2019, **26**(7), 637–648.
76 D. K. Klimov and D. Thirumalai, Dissecting the assembly of Abeta16-22 amyloid peptides into antiparallel beta sheets, *Structure*, 2003, **11**(3), 295–307.
77 D. Thirumalai, A. Kumar, D. Chakraborty, J. E. Straub and M. L. Mugnai, Conformational fluctuations and phases in fused in sarcoma (FUS) low–complexity domain, *Biopolymers*, 2023, e23558.
78 G. Krainer, T. J. Welsh, J. A. Joseph, J. R. Espinosa, S. Wittmann, E. de Csillery, A. Sridhar, Z. Toprakcioglu, G. Gudiskyte, M. A. Czekalska, *et al.*, Reentrant liquid condensate phase of proteins is stabilized by hydrophobic and non-ionic interactions, *Nat. Commun.*, 2021, **12**(1), 1085–1098.
79 J. A. Joseph, A. Reinhardt, A. Aguirre, P. Y. Chew, K. O. Russell, J. R. Espinosa, A. Garaizar and R. Collepardo-Guevara, Physics-driven coarse-grained model for biomolecular phase separation with near-quantitative accuracy, *Nat. Comput. Sci.*, 2021, **1**(11), 732–743.
80 R. M. Vernon, P. A. Chong, B. Tsang, T. H. Kim, A. Bah, P. Farber, H. Lin and J. D. Forman-Kay, Pi-Pi contacts are an overlooked protein feature relevant to phase separation, *eLife*, 2018, **7**, e31486.
81 J. M. Choi, A. S. Holehouse and R. V. Pappu, Physical Principles Underlying the Complex Biology of Intracellular Phase Transitions, *Annu. Rev. Biophys.*, 2020, **49**, 107–133.
82 E. W. Martin, A. S. Holehouse, I. Peran, M. Farag, J. J. Incicco, A. Bremer, C. R. Grace, A. Soranno, R. V. Pappu and T. Mittag, Valence and patterning of aromatic residues determine the phase behavior of prion-like domains, *Science*, 2020, **367**, 694–699.
83 G. Reddy, J. E. Straub and D. Thirumalai, Dry amyloid fibril assembly in a yeast prion peptide is mediated by long-lived structures containing water wires, *Proc. Natl. Acad. Sci. U. S. A.*, 2010, **107**(50), 21459–21464.